Dynamic Current and Power Distributions in a Submerged Arc Furnace

Y. A. Tesfahunegn[1], T. Magnusson[2], M. Tangstad[3] and G. Saevarsdottir[4]

[1] School of Science and Engineering, Reykjavik University, Menntavegur 1, 101 Reykjavik, Iceland. Email: yonatant@ru.is. Tel. +354 599-6587

[2] United Silicon, Stakksbraut 9, 230 Reykjanesbæ, Iceland. Email: tm@silicon.is. Tel. +354 669 6004

[3] Department of Materials Science and Engineering, NTNU, N-7491 Trondheim, Norway. Email: merete.tangstad@ntnu.no. Tel. +47 97180255

[4] School of Science and Engineering, Reykjavik University, Menntavegur 1, 101 Reykjavik, Iceland. Email: gudrunsa@ru.is Tel. +354 5996345

Abstract

Most submerged arc furnaces used for the production of ferroalloys run on three-phase alternating current. This affects the electrical operation of the furnace and thus it is of interest to study alternating current distributions in the system. This work presents computations of alternating electric current distributions inside an industrial submerged arc furnace for silicon production. A 3D model has been developed in ANSYS Maxwell using the eddy current solver. In each phase, electrode, central arc, crater, crater wall and side arcs that connect electrode and crater wall are taken into account. In this paper, the dynamic current distributions in different parts of the furnace, as well as skin and proximity effects in and between electrodes are presented. Moreover, active and reactive power distributions in various components of the furnace are quantified.

Keywords: Current distribution, Current paths, Power distributions, Submerged arc furnace.

1. Introduction

The current distribution in the submerged arc furnace is critical to good operation in the silicon metal production process. Phase current or resistance are among the most important control parameters, but for modern silicon metal or ferrosilicon furnaces there is no mechanism to measure the actual current distribution. Metallurgists operate the furnaces based on the analysis of limited data at hand. Recent dig-outs of industrial furnaces have expanded available information on location-dependent charge properties, this enables more realistic modelling of electrical conditions in the furnace than previously possible. Having proper data makes the developed numerical models reliable in predicting the furnace behavior. This will enhance the understanding of critical process parameters and allow more accurate furnace control.

The current distribution is not well known for silicon furnaces and cannot be directly measured. Sævarsdottir [1] calculated that the arc could be a maximum of 10-15cm in length, based on magnetohydrodynamics (MHD) arc modelling. Although there have been publications on this subject [2], results from an accurate model where the current distribution can be calculated have not been published to date.

The geometry of the zones in a silicon furnace is dependent on the operation history, and hence a number of different geometries, sizes and compositions are possible in the various parts of the furnace. A report from recent excavations of industrial furnaces published by Tranell et al. [3] described the various zones in a FeSi furnace. Myrhaug [4] reported similar features from a pilot scale excavation operating around 150 kW. Tangstad et al [5] published results from excavation of industrial furnaces, where the interior of the furnace is divided into zones depending on the materials and their degree of conversion. Mapping the material distribution gives a basis for quantifying the location dependent physical properties of the charge materials such as the electrical conductivity.

Complete numerical modeling of submerged arc furnace (SAF) requires electrical, chemical, thermal and fluid flow considerations. In this paper, we only consider the electrical aspect, which needs electrical conductivity of the different parts of the furnace. Some works have been done to address this issue. Krokstad [6] outlined an experimental method and published data on the electrical conductivity of silicon carbide and Vangskåsen [7] looked in detail at the metal producing mechanisms. Molnas [8] and Nell [9] have also published data on dig-out samples and material analysis that are relevant. These are some of the essential inputs necessary to set up a reasonably realistic modeling domain with correct physical properties to model the current and power distributions within a furnace, and this opens a unique opportunity to create a model which enables understanding of the current and power distributions in the furnace. These results can be used in the development of furnace control strategies that can enable improved silicon recovery and current efficiency.

The recent developments of electrical numerical modeling include several features of the furnace. Tesfahunegn et al. [10, 11] developed a 3D numerical furnace model that contains electrodes, main arcs, side arcs, crater wall, crater, and other parts using ANSYS Fluent electric potential solver. The authors showed results for current distribution with or without taking into account the main arc. As a continuation of their work, they have implemented a vector potential method using a user-defined function in ANSYS Fluent environment to calculate dynamic current distributions [12, 13]. Their model is only able to consider electrodes and capable of predicting skin and proximity effects. Other researchers have developed different numerical models for SAF based on Computational Fluid Dynamics (CFD) and Finite Element Method (FEM). Herland et al. [14] studied proximity effects in large FeSi and FeMn furnaces using FEM. In their model, they have included different parts of the furnaces. Diahnaut [15] presented computations of electric field in SAF using CFD. The author showed the effect of contact resistance by studying the contact between two coke particles before dealing with a full-scale furnace. The furnace is partitioned in layers to consider different materials and no assumption has been made on the current path. Bezuidenhout et al. [16] applied CFD on a three-phase electric smelting furnace to investigate the electrical aspects, thermal and flow behavior. They showed relationships between electrode positions, current distribution and slag electrical resistivity. Darmana et al. [17] developed a modeling concept applicable for SAFs using CFD that considers various physical phenomena such as thermodynamics, electricity, hydrodynamics, heat radiation and chemical reactions. Wang et al. [18] investigated the thermal behavior inside three different electric furnaces for MgO production.

This paper presents computations of alternating current and power distributions inside an industrial submerged arc furnace for silicon metal production. A 3D model has been developed in ANSYS Maxwell [19] using the eddy current solver. Electrode, main arc, crater, crater wall, and side arc that connects the electrode and crater wall are taken into account for each phase. Other furnace parts such as carbon block, steel shell, and aluminum block are also incorporated.

2. The process

In the silicon production process, quartz and carbon materials, that are called charge, are fed into a submerged arc furnace. Three electrodes penetrate the charge from above. Electric heating from the current provides the energy to charge through the electrodes, each of which carries one of the three phases of 50 Hz AC current, canceling out at a star point in the charge.

The overall reaction for producing Silicon metal is:

$$SiO_2 + 2C = Si + 2CO(g) \tag{1}$$

This reaction, however, takes a series of sub-reactions, changing the properties of the charge along the way as intermediary reaction products are formed. The current passes from the electrodes through the raw-material charge and an electric arc burning at the tip of the electrode. The arc, which consists of thermal plasma in the range of 10000-20000K [20], provides heat for energy-consuming silicon-producing reaction (4), while the SiC-forming reaction and SiO(g) condensation reactions (2) and (3) take place at a lower temperature higher up in the furnace, see Schei et. Al [21].

$$SiO(g) + 2C = SiC + CO(g) \tag{2}$$
$$2SiO(g) = Si + SiO_2 \tag{3}$$
$$SiO_2 + SiC = SiO(g) + CO(g) + Si(l) \tag{4}$$

It is essential for the silicon recovery in this process that there is a balance between the high-temperature reactions (4) and the low- temperature reactions (2) and (3). Therefore, it is necessary that sufficient heat is released in the arc to drive reaction (4), while a certain part should be released in the raw-material charge to drive reaction (2). The stoichiometry of reaction (4) is affected by temperature, and the ratio is decreased at higher temperature, which above 1900°C enables a high silicon recovery. In the silicon process it is the electric arc that creates sufficiently high temperature; therefore, sufficient arcing is important for good silicon recovery.

3. Computational Model

In this section, we describe the mathematical modeling, the furnace geometry, material properties, mesh generation and boundary conditions.

3.1 Mathematical modeling

In this paper, we will focus only on the electrical aspects of SAF. The 3D electrical model is developed in ANSYS Maxwell [19] using eddy current solver, which is suitable for low-frequency devices and phenomena. It solves sinusoidally-varying magnetic fields in the frequency domain. The frequency domain solution assumes frequency to

be the same throughout the domain. Induced fields such as skin and current proximity effects are also considered. It is a quasi-static solver. To solve for the magnetic field, H, the solver computes the values as follows [19]:

$$\nabla \times \left(\frac{1}{\sigma + j\omega\varepsilon} \nabla \times H\right) = -j\omega\mu H \tag{5}$$

where σ, ω, μ and ε are electrical conductivity, circular frequency, magnetic permeability and electrical permittivity. The magnetic permeability is typically given by $\mu = \mu_r\mu_0$, where $\mu_0 = 4\pi \times 10^{-7}$ [H/m] is the constant magnetic permeability of vaccum and μ_r [-] is the relative magnetic permeability. Once Eq. (5) is solved, the electrice field (E) and the electric current densitry (J) are solved using Faraday's and Ampere's laws. Also, J and E are related by Ohm's law. The equation is solved using the finite element method.

3.2 Furnace geometry and material properties

The computational domain is based on the actual design of a 32 MW industrial furnace with AC frequency of 50 Hz. A simplified schematic drawing of the furnace is shown in Fig. 2. The furnace is partitioned into different zones based on the material properties. Included in the modeling are the furnace lining, three electrodes, charge, molten material, three arcs below electrodes, side arcs, three craters with crater walls made of carbides. The geometry of each electrode is considered as a truncated right conical shape. The upper surface of the electrode is the base of the cone with radius equals to the radius of the electrode. The radius of the bottom surface of the electrodes changes as the slope of the slant height changes. We assume that several concentrated side-arcs are distributed around the circumference of the electrode near the tip electrodes, and the circular distances between each side-arc are held constant. With this configuration, the number of side-arcs increases linearly with the circumference of the electrode.

For brevity, a section of the furnace and one electrode are depicted in Fig. 2. For each phase, two types of arcs are introduced. The main-arc, burning below the electrode, with an arc length of 10 cm and diameter of 5cm [2], and some shorter side-arcs connecting the crater wall to the side of the electrode. The curvature of the three crater walls is assumed to be a circular section with a diameter of 100 cm [22]. Each of the zones is assumed to have constant electrical conductivity. The conductivity of each zone is taken from various literature sources and summarized in Table 1.

Table 1. Electrical conductivity of different zones

Zones	Electrical conductivity [S/m]
Electrode [6]	225000
Arc [22]	7000
Crater	1e-14
Carbide [6]	400
Charge	0.15, 15
Molten material [23]	1388900
Carbon block [6]	225000
Alumina brick	1e-14
Steel shell [14]	6.3e+10
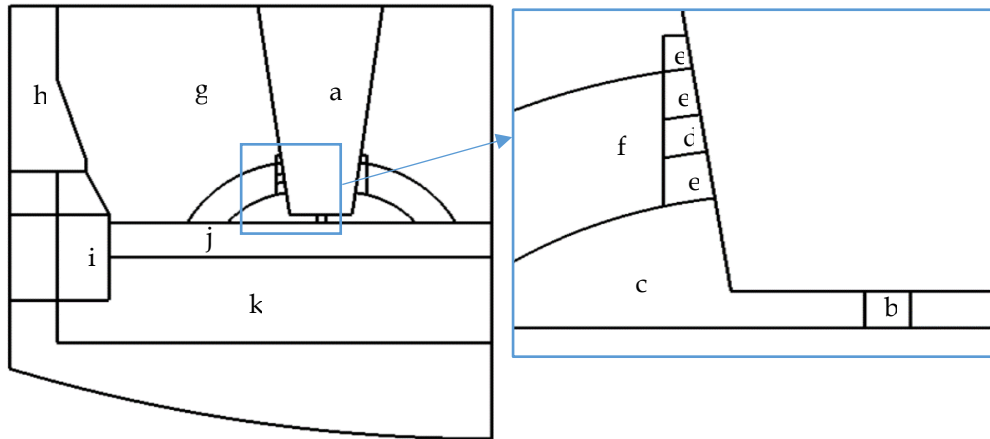
Figure 2. Schematic of the industrial Silicon SAF with different zones (a) electrode, (b) arc, (c) crater, (d) side arc, (e) gap, (f) carbide, (g) charge, (h) alumina brick, (i) carbon block and carbide, (j) molten material, and (k) carbon block.

3.3 Mesh generation and boundary conditions

Mesh generation is a crucial part of any computational method. It has a significant influence on the runtime and memory use of simulation, as well as the accuracy and stability of the solution. Since the eddy current solver utilizes an adaptive mesh refinement algorithm, the material volumes described in Section 3.2 were meshed according to the method. This type of meshing technique provides automated mesh refinement capability based on reported energy error in simulation.

The model boundary conditions were imposed based on the positions of the surfaces in the model. Two types of boundary conditions are required, i.e., the natural and Neumann. The natural boundary condition is used for interface between objects. It describes the natural variation from one material to the next one, as defined by material property. The Neumann boundary condition is applied for exterior boundary of solution domain and the H field is tangential to the boundary and flux cannot cross it. To impose appropriate boundary conditions on the H field, a large far-field around the furnace which is filled with air is created. The top surface of the three electrodes are excited by current with equivalent value of $I_{rms} = 99\ kA$. The phase shift between electrodes is 120°.

4. Numerical cases

In this section, we determine the current and power distributions inside the furnace described in Section 3.2 as well as other parameters, such as resistance, power factor, and voltage of the system. We consider three factors. The first factor is the number of side-arcs with two levels (8 and 14), the second aspect is the charge conductivity with two levels (0.15 and 15 S/m) and the third element is the consideration of the main arcs with two levels (with main arcs and without main arcs). Hence, a total of 8 simulation cases have been performed. For discussion purposes, we group them into two categories based on the third factor. We only vary the other two factors, i.e., number of side arcs and charge conductivity. The two categories are summarized in Table 2.

Table 2: Two simulation groups

Category	Number of side-arcs		Charge conductivity	
	8	14	0.15 S/m	15 S/m
Main arcs	✓	✓	✓	✓
No main arcs	✓	✓	✓	✓

For all cases, the phase current has the same value. This means that with changing domain configuration the total resistance changes, and thus the voltage fo the system. Some of the cases represent realistic phase resistance in the system while others do not, the goal with this effort is to gain a qualitative understanding of the governing mechanisms for the current and power distributions in the system. For all cases, the simulations were performed by adaptive meshing algorithm using energy error as a convergence criterion. The energy error set to 2 percent. For all cases, the initial mesh size is ~ 0.7e+06 elements and the simulation is converged the mesh size is ~1.5e+06 elements. The simulation time per a case on average is around 3 hrs.

Since the results that are required for this study are not directly obtained from the simulation, we need to perform post-processing. The current is calculated from current density by integrating on the surface of interest. The active power density, $p\ [W/m^3]$, given by $p = |J|^2/2\sigma$, and the reactive power density $q\ [W/m^3]$, given by $q = (\pi f/\mu)|B|^2$. By integrating the respective power densities over different material domain and the entire furnace, we obtain active power, $P[MW]$ and reactive power, $Q[MW]$. Once the active and reactive powers of the furance are calculated, others results such as power factor (PF) and resistance (R) of the system can be calculated.

Figure 3 shows the resulting nonuniform current density on the three electrodes due of skin and proximity effects. Figure 4 shows the total current through electrode and the main arc at different height of the furnace. The vertical axis is a normalized current, which is the fraction of the phase current in the electrode and arc. The horizontal axis is dimensionless furnace height, which is the ratio between a given height and the total height of the furnace. In this paper, we define the total height of the furnace from the bottom of the furnace to the top of the electrodes. In Fig. 4a main arc is considered whereas in Fig. 4b is not included. In both figures the charge conductivity and the number of side arcs are varying as shown in Table 2. Irrespective of the magnitude of reduction, the current is decreasing from the top of the electrode to the bottom as the charge conductivity increases. Moreover, the current passed to the main-arc (Fig. 4a) is also decreased as the number of side arcs are increased.
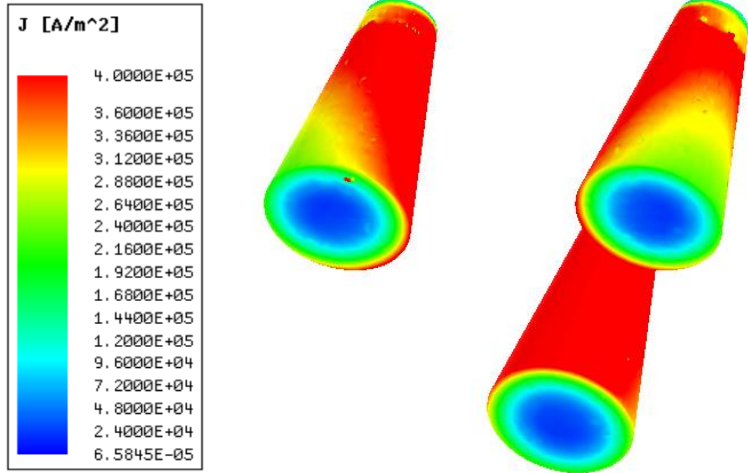
Figure 3. Current density in the electrodes
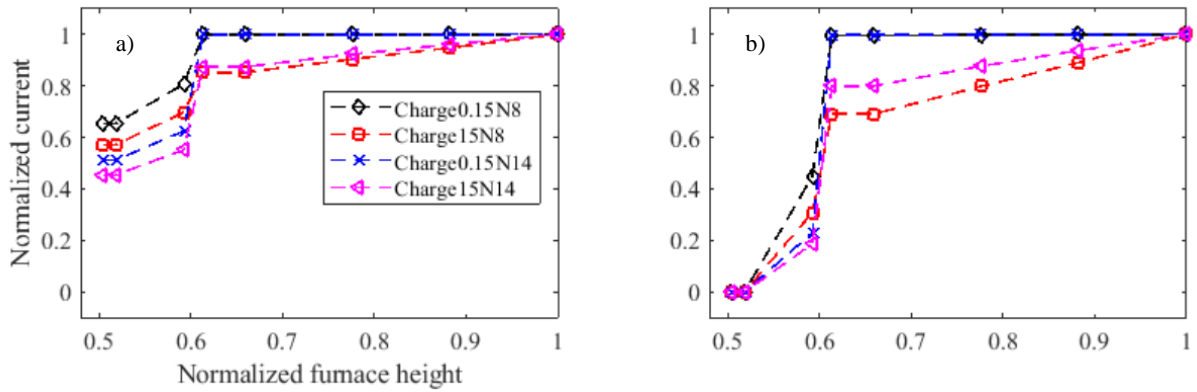
Figure 4. Normalized current passing through electrode and main arc as a function of normalized height from the furnace bottom to the top of electrodes: (a) with main-arc, and (b) without main-arc

Table 3 shows the active and reactive power distributions in different zones for eight side arcs with and without main arcs consideration. Besides the charge conductivity is varying. When the main-arcs are included and charge conductivity is low, most of the power is accumulated in the main arcs and crater wall, while some power is deposited in the remaining zones. However, when the charge conductivity is changed by order of two magnitudes, the active power in the charge is increased by the same order of magnitude while decreasing in the main arcs and crater wall. Without the main-arcs, we can see the same trend except for no power in the main arcs. The main contributors to the reactive power are the far-field, charge, and electrodes. The other materials have some contributions. Since we have not included the electric components outside the furnace, such as bus bars and flexibles, the total value of the reactive power could be higher than the reported values. The simulation results for the 14 side arcs are not reported as in Table 3 since we saw the same trend. Instead, the results are summarized for all simulations results as shown in Table 4. Having main arcs show that resistance of the system is sensitive to the change of charge conductivity and the number of side arcs. Without the main arcs, the resistance in the furnace is increased by 100-150%, compared with corresponding simulation cases (Table 4). Most furnaces are operated to strive towards constant resistances. The variations in conductivity conditions in the furnace are met by moving the electrodes up and down. From these simulations we see how the phase resistance can change with either the conductivity of the charge is changed and (or) exist main arcs and(or) side-arcs. One of the assumptions that we made in the simulations is that for each case the charge conductivity is uniform. In a real furnace, however, the charge conductivity is increasing as it moves from the top of the furnace to the bottom. Overall the trend that can be observed is that increasing the system conductivity will result in a reduction of the system resistance.

Table 3 Active and reactive power distributions in different zones for eight side arcs setup

Zones	With main arcs				No main arcs			
	Charge cond. 0.15		Charge cond. 15		Charge cond. 0.15		Charge cond. 15	
	P [MW]	Q [MW]	P [MW]	Q [MW]	P [MW]	Q [MW]	P [MW]	Q [MW]
Electrode	2.36	1.88	2.15	1.75	2.07	1.73	1.80	1.55
Main arcs	23.07	0.02	17.25	0.02	0.00	0.00	0.00	0.00
Side arcs	0.55	0.00	0.38	0.00	4.64	0.00	2.24	0.00
Crater wall	10.30	0.42	7.42	0.32	83.94	0.25	40.23	0.13
Crater	0.00	0.40	0.00	0.30	0.00	0.11	0.00	0.06
Charge	0.06	6.79	4.64	5.84	0.45	6.78	20.30	4.88
Molten Si	0.15	0.13	0.12	0.10	0.06	0.07	0.04	0.04
Carbon block	0.03	0.03	0.03	0.02	0.03	0.03	0.03	0.02
Farfield	0.00	13.00	0.00	13.00	0.00	13.00	0.00	12.99
Steel Shell	0.01	0.14	0.01	0.14	0.01	0.15	0.01	0.13
Alumina brick	0.00	0.18	0.00	0.17	0.00	0.18	0.00	0.16
Total	36.53	23.00	32.00	21.66	91.18	22.29	64.63	19.97

Table 4 Summary of power distributions and other results of all cases

Cases	With main arcs				No main arcs			
	P [MW]	Q [MW]	PF [ ]	R [mΩ]	P [MW]	Q [MW]	PF [ ]	R [mΩ]
Charge0.15_ Nside8	36.53	23.00	0.85	1.24	91.18	22.29	0.97	3.10
Charge15_ Nside8	32.00	21.66	0.83	1.09	64.63	19.74	0.96	2.20
Charge0.15_ Nside14	29.00	21.23	0.81	0.99	51.39	20.73	0.93	1.75
Charge15_ Nside14	25.77	20.37	0.78	0.78	40.19	19.50	0.9	1.37

5. Conclusions

This paper presents computations of dynamic current and power distributions inside an industrial submerged arc furnace for silicon production. A 3D model has been developed in ANSYS Maxwell using eddy current solver. Electrodes, main arcs, crater, crater wall, and side-arcs that connect electrode and crater wall are considered for each phase. In this paper, the current distributions in the electrodes and main-arcs and the power distributions in different parts of the furnace are presented by varying the charge conductivity, the number of side arcs and with and without main-arcs. The presented model is able to capture skin and proximity effects. It was observed that the resistance of the furnace is sensitive to changes in charge conductivity, number of side arcs and existence of main-arcs. When exist main-arcs are present, most of the power is accumulated in the main-arcs and crater wall for both high and low charge conductivities. It is the conductivity in the crater wall that determines the resistance in the volume at the side-arc attachment and limits the side-arc current. Thus, without main-arcs, a significant portion of the power is placed in the crater and charge depending on the charge conductivity value, but the overall resistance in the system is unrealistically high. It is seen that most of the reactive power in the furnace resides in the charge and far-field and depends on the overall current in the system. It is observed that a more narrow current path tends to increase the reactive power in the furnace and thus reduce the power factor. However as the phase resistance and thus real-power dissipation is much more sensitive to the current path, the power factor is much higher for the cases without the presence of main-arc.

References

1. Sævarsdottir GA, Bakken JA, Sevastyanenko VG, Liping Gu (2011) High power ac arcs in metallurgical furnaces. High Temperature Material Processes, Volume 15, Issue 3.

2. Saevarsdottir GA, Bakken JA (2010) Current distribution in submerged arc furnaces for silicon metal / ferrosilicon production, In proceedings INFACON12.

3. Tranell G, Andersson M, Ringdalen E, Ostrovski O, Stenmo JJ (2010) Reaction zones in a FeSi75 furnace – results from an industrial excavation. INFACON XII, 709-715.

4. Myrhaug EH (2003) Non-fossil reduction materials in the silicon process -properties and behavior. Ph.D. thesis, NTNU.

5. Tangstad M, Ksiazek M, Andersen J E (2014) Zones and materials in the Si furnace, In proceedings: Silicon for the Chemical and Solar Industry XII, Trondheim, Norway, June 24-27.

6. Krokstad M (2014) Electrical resistivity of industrial SiC crusts, MSc-thesis NTNU.

7. Vangskåsen J (2012) Metal-producing mechanisms in the carbothermic silicon process. MSc. thesis, NTNU.

8. Mølnås H (2010) Investigation of SiO condensate formation in the silicon process, Project report in TMT 4500, NTNU, Norway.

9. Nell J, Joubert C (2013) Phase Chemistry of digout samples from a ferrosilicon furnace, Infacon prceedings Kazakhstan.

10. Tesfahunegn YA, Magnusson T, Tangstad M, Saevarsdottir G (2018) Effect of electrode shape on the current distribution in submerged arc furnaces for silicon production- A modelling approach. J. South. Afr. Inst. Min. Metall. 118 (6): 595-600

11. Tesfahunegn, YA, Magnusson, T, Tangstad, M, Saevarsdottir, G (2018) Effect of carbide configuration on the current distribution in submerged arc furnaces for silicon production—A modelling approach. In: Nastac L., Pericleous K., Sabau A., Zhang L., Thomas B. (eds) CFD Modeling and Simulation in Materials Processing 2018. TMS 2018. The Minerals, Metals & Materials Series. Springer, Cham, p 175-185

12. Tesfahunegn, YA, Magnusson, T, Tangstad, M, Saevarsdottir, G (2018) Dynamic current distribution in the electrodes of submerged arc furnace using scalar and vector potentials. In: Shi Y. et al. (eds) Computational Science – ICCS 2018. ICCS 2018. Lecture Notes in Computer Science, vol 10861. Springer, Cham, p 518-527

13. Tesfahunegn, YA, Magnusson, T, Tangstad, M, Saevarsdottir, G (2018) The effect of frequency on current distributions inside submerged arc furnace. Paper presented at the IEEE MTT-S International Conference on Numerical and Electromagnetic and Multiphysics Modeling and Optimization, Reykjavik, Iceland, 08-11 August 2018.

14. Herland EV, Sparta M, Halvorsen SA (2018) 3D models of proximity effects in large FeSi and FeMn furnaces. J. South. Afr. Inst. Min. Metall. 118 (6): 607-618

15. Dhainaut M (2004) Simulation of the electric field in a submerged arc furnace. INFACON X, 605- 613.

16. Bezuidenhout JJ, Eksteen JJ, Bardshaw SM (2009) Computational fluid dynamic modelling of an electric furnace used in the smelting of PGM containing concentrates. Minerals Engineering 22: 995-1006. https://doi.org/10.1016/j.mineng.2009.03.009

17. Darmana D, Olsen JE, Tang K, Ringldalen E (2012) Modelling concept for submerged arc furnaces. Paper presented at the Ninth International Conference on CFD in the Minerals and Process Industries CSIRO, Melbourne, Australia, 10-12 December.

18. Wang Z, Fu Y, Wang N, Feng L (2014) 3D numerical simulation of electrical arc furnaces for the MgO production. J. Mat. Pro. Tec. 214: 2284-2291. http://dx.doi.org/10.1016/j.jmatprotec.2014.04.033

19. Maxwell, ver. 18.0 (2018) ANSYS Inc., Southpointe, 275 Technology Drive, Canonsburg, PA 15317.

20. Saevarsdottir GA, Bakken J., Sevastyanenko V, Liping G. (2001) Arc simulation model for three-phase electro metallurgical furnaces. INFAXCON IX. Proceedings of the 12th International Ferroalloys Congress, Quebec City, Canada.

21. A.Schei, J.K.Tuset, H.Tveit (1998) Production of high silicon alloys.Tapir Forlag, Trondheim.

22. Sævarsdottir GA (2002) High current ac arcs in silicon and ferrosilicon furnaces. Ph.D. thesis, NTNU.

23. Sasaki H, Ikari A, Terashima K, Kimura S (1995) Temperature Dependence of the Electrical Resistivity of Molten Silicon. Jpn. J. Appl. Phys. https://doi.org/10.1143/JJAP.34.3426